Available online at www.sciencedirect.com
ScienceDirect
Trans. Nonferrous Met. Soc. China 35(2025) 1262−1280
Transactions of Nonferrous Metals Society of China
www.tnmsc.cn

Thin layers of Fe-doped ZnO deposited by spin-coating for electrolysis and photodetector applications

Dikra BOURAS[1], Mamoun FELLAH[2,3], Régis BARILLÉ[4], Amjad IQBAL[5], Hamadi FOUZIA[3,6], Obrosov ALEKSEI[7], Gamal A. EL-HITI[8]

1. Faculty of Science and Technology, University of Souk-Ahras, Algeria;
2. Mechanical Engineering Department, ABBES Laghrour University, Khenchela PO 1252, CP 40004, Algeria;
3. Biomaterial, Synthesis and Tribology Research Team, ABBES Laghrour-University, Khenchela, P.O 1252, 40004, Algeria;
4. MOLTECH-Anjou, Université d'Angers/UMR CNRS 6200, 2 Bd Lavoisier, 49045 Angers, France;
5. Department of Materials Technologies, Faculty of Materials Engineering, Silesian University of Technology, Krasińskiego 8, 40-019, Katowice, Poland;
6. Matter Science Department, ABBES Laghrour University, Khenchela PO 1252, CP 40004, Algeria;
7. Brandenburg University of Technology Cottbus-Senftenberg, 03046, Cottbus, Germany;
8. Department of Optometry, College of Applied Medical Sciences, King Saud University, Riyadh 11433, Saudi Arabia

Received 2 September 2023; accepted 26 March 2024

Abstract: The effect of iron concentration on the microstructural and structural properties of ZnO for electrolysis and photodetector applications was investigated. The thin layers of un-doped and doped ZnO with different percentages of Fe (2, 4, and 6 wt.%) were deposited by spin-coating on glass substrates. Sample characterization was done by X-ray diffraction (XRD), atomic force microscopy (AFM), scanning electron microscopy (SEM), energy-dispersive X-ray spectroscopy (EDS), UV−Vis absorption spectra and X-ray photoelectron spectroscopy (XPS). Structural measurements by XRD showed that all the layers were composed of polycrystallines with a hexagonal Wurtzite structure. Two new peaks were also discovered after the doping process belonging to the Fe_2O_4 (400) and (440) crystal phase. Morphological analysis showed that the surface roughness values of ZnO layers ranged between 8 and 45 nm. XPS studies confirmed the presence of Fe in 3+ states in ZnO layers. An average transmittance of 90% was measured by UV−Vis in the wavelength range of 200−900 nm. The values of the energy gap (E_g) decreased with an increase in the concentration of Fe. AFM topography results confirmed that ZnO-based thin layers had a relatively uniform surface. The efficiency of these samples has been confirmed for their use in many electrical applications, including photodetectors and electrolysis of contaminated solutions.

Key words: Fe:ZnO; gap energy; electrolysis; photodetector; efficiency

1 Introduction

ZnO is nowadays used not only as an additive for the copper and cement industry, but also in medicine and cosmetic industry as part of the substitute materials of choice for the field of new technologies such as renewable energy [1,2]. With the rise of electronics, opto-electronics, and photovoltaic technologies, studies on the use of ZnO as a semiconductor have significantly increased, with the aim of taking advantage of its unique physical and chemical properties. Since the 1930s, ZnO has experienced a growing interest

Corresponding author: Mamoun FELLAH, E-mail: mamoun.fellah@yahoo.fr, mamoune.fellah@univ-khenchela.dz
DOI: https://doi.org/10.1016/S1003-6326(24)66747-6

until the 1970s for its potential application in opto-electronics [3].

The possibility of synthesizing ZnO single crystals and epitaxial layers of high quality exhibiting strong luminescence added to the diversity of accessible nanostructures has motivated a strong resurgence of interest in the scientific community towards this material since the mid-1990s [4]. ZnO indeed offers strong potential applications considering its wide direct energy gap of 3.37 eV at room temperature, with a high exaction binding energy of 60 meV, allowing intense, exciting emission at room temperature, strong piezoelectric properties, as well as high electron mobility, up to 200 $cm^2 \cdot V^{-1} \cdot s^{-1}$ [5].

The abundance of zinc also stimulates this interest, as do the low production costs of ZnO, its low toxicity, and its biocompatibility [6]. These advantages naturally lead to the consideration of ZnO as an alternative to GaN for opto-electronics in the blue and UV range. In addition, its good transmittance in the visible, greater than 85%, associated with a satisfactory electrical resistivity of the order of $10^{-4}\,\Omega \cdot cm$ for ZnO doped with aluminum, makes it possible to consider the use of ZnO thin films as transparent conductive oxide, in particular as a replacement for In_2O_3:Sn (ITO) [7]. ZnO is also useful for space applications because of its resistance to radiation, which is typically stronger than other common semiconductors (Si, GaAs, CdS, and GaN) [8].

The current interest around ZnO is partly fueled by the very wide variety of nanostructures that can be obtained with low-cost and easy-to-implement elaboration methods [9]. Nanowires, nanorods, nanoneedles, nanotubes, nano-helices, nano-flakes, nano-rings, nano-ribbons, and nano-combs of ZnO have thus been synthesized [10]. This unique characteristic of ZnO is notable for the large number of review articles published over the past twenty years devoted to synthesis, properties, and applications of these nanostructures [11].

There has also been great interest in dilute transition metal (TM) magnetic semiconductors due to the possibility of manipulating their charge and spin degrees of freedom. The doped diluted magnetic semiconductors (DMSs) are potential candidates for the next generation of spin electronic devices, such as spin diode transistors, light-emitting diodes, non-volatile storage devices, and logic devices [12]. ZnO doped with transition metals as dopants, such as Ni, Co, Mn, and Fe, has been widely studied with the aim of modifying magnetic properties for potential applications in spintronic devices [13].

Ferromagnetism was focused on studying zinc oxide doped with iron [14]. Few works have systematically explored the optical properties of ZnO after Fe doping [15]. HAN et al [16] showed that both X-ray diffraction and X-ray photoelectron spectroscopy analysis displayed that Fe atoms were successfully incorporated into the ZnO thin films and existed in the form of Fe^{2+} mostly in 1 at.% Fe-doped ZnO films, and mainly existed in the form of Fe^{3+} in higher concentrations of films. Undoped and Fe-doped zinc oxide (ZnO) nanofibers were prepared by the electrospinning method to investigate effect of transition metal ion doping on photocatalytic performance of ZnO [17,18].

It was realized that the crystallization of ZnO fibers was significantly improved by optimizing the sintering conditions [19]. One of the most important reasons for choosing Fe as a suitable dopant is that it has the effective ionic radius of Fe^{2+} (0.76 Å) and Fe^{3+} (0.64 Å) similar to that of Zn^{2+} (0.74 Å), which helps to organize and reduce the distortion of the crystal lattice of iron-doped zinc oxide to some extent [14,20]. On the other hand, the chemical state of iron ions plays an important role in modifying the energy range. The replacement of Zn ions by Fe would introduce some impurity levels and enrich the energy level structure. The valence states of Fe^{2+} and Fe^{3+} present in Fe-doped ZnO can lead to both synergy and competition effects.

VIRDIAN et al [21] synthesized Fe-doped ZnO thin films by the direct current reactive magnetron co-spraying method, but experiments showed that Fe doping can severely affect the structural and physical properties primarily due to changing the valence state of Fe from Fe^{3+} to Fe^{2+}. WANG et al [22] prepared a series of Fe-doped ZnO films using a target-facing magnetron sputtering system, and the results showed that Fe was in two valence states.

The synthesis of ZnO thin layers doped with magnetic ions is demonstrated by spin-coating deposition [23], along with many other chemical and physical deposition techniques such as dip-coating [24], Spray coating, electrochemical deposition [25], chemical vapor deposition [26]

assisted or not by the vapor-liquid-solid (VLS) process [27] and physical vapor deposition (PVD) [28]. These nanostructures typically benefit from excellent crystalline quality with good electrical charge transport properties [29,30]. Moreover, its magnetic properties depend on the method of preparation, stoichiometric conditions, temperature, raw materials, and pH. Their high form factor allows large, developed surfaces and gives a high chemical reactivity and a high sensitivity to surface effects. These advantages can be used for a number of applications, such as sensors and detectors [31].

Nanostructures have thus been integrated into solar cells, including dye cells [32], extremely thin absorber cells [33], quantum wells [34], or in combination with perovskites [35]. In these cases, ZnO nanowires are considered as an alternative to layers based on TiO_2 nanoparticles due to a higher mobility of electrons in ZnO than in TiO_2 (200 $cm^2 \cdot V^{-1} \cdot s^{-1}$ against 1 $cm^2 \cdot V^{-1} \cdot s^{-1}$, respectively), and their monocrystalline character, allowing a direct electrical conduction path [36]. Very popular applications with ZnO include UV photo-detectors [37], piezoelectric nano-generators [38], gas sensors [39], as well as light-emitting diodes (LEDs) [40], transistors [41], and biosensors [42].

In this study, Fe-doped ZnO thin films were prepared with different concentrations of Fe doping (2, 4, and 6 wt.%) by the spin-coating method. The doping effect of Fe has been studied to improve the structural, morphological, and conductivity properties of ZnO thin layers. Two applications are presented based on Fe-doped ZnO samples. The first one, the photodetector method, allows knowing the sensitivity of thin layers in the dark and under ultraviolet light. It was confirmed with this method that the photocurrent of the photodetectors for Fe:ZnO samples has significant photosensitivity to UV light compared to the dark current. The second method is the electrolysis of a dye (Methylene blue) using thin layers and by applying an electric current. During this process, many ions (Zn^{2+} and Fe^{2+}) are created, which disassemble and degrade the organic compound and release carbon dioxide.

2 Experimental

The doped zinc acetate ($Zn[CH_3COO]_2 \cdot 2H_2O$) (purity: 98%) (3.046 g) with different quantities of iron ($FeCl_3$, H_2O) (purity: 97%) (0, 2, 4 and 6 wt.%), was first prepared by dissolving in a solution of ethanol (C_2H_5OH) (purity: 99.8%) and ethanolamine [$NH_2CH_2CH_2OH$] heated at 70 °C with a heating plate. The concentration of zinc acetate was maintained at 0.4 mol/L.

Before depositing the prepared solution on the glass substrate, a value pH was calculated for the four solutions and was found to range between 5.6 and 6.79. The relationship between precursor solution viscosity and solution concentration is given in Fig. 1 for 0 wt.% Fe, 2 wt.% Fe, 4 wt.% Fe and 6 wt.% Fe shows that the viscosity increases with increasing concentration [43]. The viscosity value changed from 0.025 Pa·s for the pure ZnO to 0.034 Pa·s for 6 wt.% Fe doped ZnO (6 wt.% Fe:ZnO). This could lead to the doping of the initial solution, affecting the structural and optical properties of the studied thin layers [44].

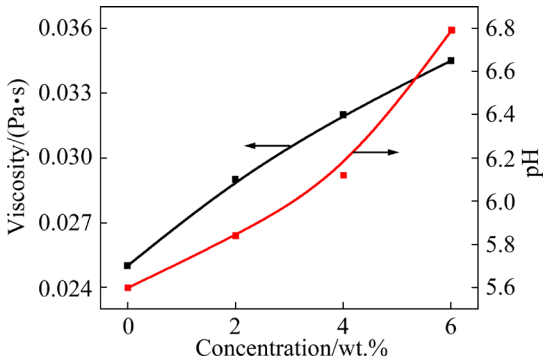

Fig. 1 Relationship between viscosity, pH and concentration of solutions of ZnO, 2% Fe:ZnO, 4% Fe:ZnO, and 6% Fe:ZnO

For the preparation of thin films, a spin-coating technique was used. The prepared solution was sprayed onto the glass substrate, which was cleaned with acetone and rinsed with water for 1 min at room temperature at 100 r/min spin speed and then dried at 200 °C for 5 min. The process is repeated four times. Finally, the layers were annealed in an oven at 500 °C for 2 h. The different steps for preparing solutions and layers are illustrated in Fig. 2.

3 Results and discussion

3.1 X-ray diffraction

The results of XRD analysis with doped and undoped ZnO thin films are shown in Fig. 3. We observe in this figure, layers of hexagonal wurtzite

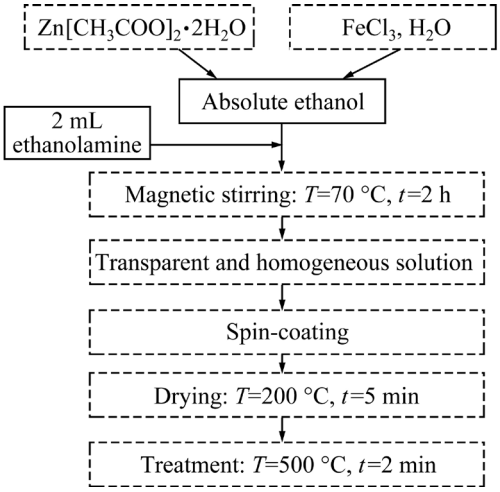

Fig. 2 Synoptic diagram showing preparation steps for Fe-doped ZnO-based thin layers using spin-coating method

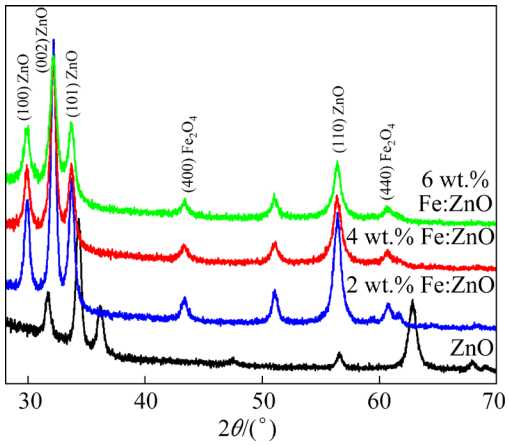

Fig. 3 Diffraction patterns of X-rays obtained for thin layers of Fe-doped ZnO

structure (JCPDS Card No. 36-1451). The crystallinity of the ZnO layers decreases when the iron doping concentration increases. Samples doped with 2 wt.%, 4 wt.%, and 6 wt.% Fe displayed additional diffraction peaks compared to samples of pure ZnO. The additional XRD peaks are (400) and (440), corresponding to the Fe_2O_4 phase (JCPDS Card No. 22-1012) [45].

The crystallinity of the ZnO layers decreases when the iron doping concentration increases. In addition, there is a shift in the position of the peaks (100), (002), (101), and (103), indicating a dilatation of the crystal lattice by the introduction of iron (Fe^{2+}: 0.55 Å) in the ZnO matrix and by substitution on a Zn site (Zn^{2+}: 0.74 Å) [46].

Table 1 gives the structural analysis results with the different compounds contained in the prepared samples. Based on the results, the average particle size was approximately obtained. It was found that the sample based on zinc oxide (ZnO) contained a smaller particle size, estimated at ~16 nm, compared to the samples doped with 2 wt.% Fe (2% Fe:ZnO) and 4 wt.% Fe (4% Fe:ZnO), which were estimated at 17 and 18 nm, respectively. However, the sample containing thin layers 6 wt.% Fe (6% Fe:ZnO) decreased in particle size, reaching ~15 nm.

Changing the proportions of doping leads to a distortion of the crystal lattice with a shift in the angles and also an increase or decrease in the intensity of the peaks [16]. This can be attributed to the merging of defective atoms in the structure due to their different ionic diameters [47]. Thus,

Table 1 Crystallite size, micro-strain and dislocation density of thin layers

Sample	Phase	(*hkl*)	2*θ*/(°)	*β*/rad	*D*/nm	Micro-strain, *ε*/%	*δ*/10^3m^{-2}
ZnO	ZnO	(100)	31.71	0.008526	16.91	0.43	3.49
	ZnO	(002)	34.31	0.008352	17.38	0.68	3.31
	ZnO	(101)	36.18	0.00957	15.24	0.42	4.3
2 wt.% Fe:ZnO	ZnO	(100)	29.94	0.0087	16.49	0.77	3.68
	ZnO	(002)	32.15	0.00783	18.43	0.39	2.94
	ZnO	(101)	33.74	0.008526	16.99	0.4	3.46
4 wt.% Fe:ZnO	ZnO	(100)	29.91	0.007134	20.12	0.47	2.47
	ZnO	(002)	32.15	0.008526	16.93	0.51	3.49
	ZnO	(101)	33.69	0.00783	18.51	0.43	2.92
6 wt.% Fe:ZnO	ZnO	(100)	29.94	0.0087	16.5	0.42	3.67
	ZnO	(002)	32.15	0.010266	14.06	0.38	5.06
	ZnO	(101)	33.67	0.009048	16.01	0.37	3.9

interstitial sites are occupied by replacement of Fe^{3+} impurity ions in the place of Zn^{2+} ionic sites in the ZnO matrix [48]. It was also observed through the increase of stress values from 0.51% to 0.58% and dislocation values from 3.31×10^3 to 5.06×10^3 m^{-2} with the increase of Fe-content in the layers from 0 to 6 wt.%. The grain particle size (D) calculation was determined by the Debye−Scherer, micro-stress (ε), and dislocation density (δ) by formulas [49,50]:

$$D=0.9\lambda/(\beta\cos\theta) \quad (1)$$

$$\varepsilon=\beta/(4\tan\theta) \quad (2)$$

$$\delta=1/D^2 \quad (3)$$

where λ is the wavelength of the anticathode (λ_{Cu}= 1.541 Å), β is the FWHM (half-value width), θ is the diffraction angle, D is the diameter of the particle size, and h, k, l are Miller indices.

The calculated values from the network are displayed in Table 2. It is noted that atomic parameters (a, b, and c) change by changing the iron ratio. This is attributed to the ionic radius of Fe^{2+} (0.55 Å) ions compared to network Zn^{2+} (0.74 Å) ions [51].

One notes that the experimental network parameters are not consistent with the theoretical parameter, which is in the JCPDS file of software instructions (00-036-1451) for zinc oxide. Based on what has been calculated, the dimension of the cell changes from one sample to another, and this is due to the contraction and expansion that occurs at the crystal network while doping the Fe element [52].

The values showed very less variation in the mesh parameters during doping with 6 wt.% Fe (a= 3.442 Å, b=3.442 Å and c=5.563 Å) compared to pure zinc oxide (a=3.257 Å, b=3.257 Å and c=5.642 Å). Changes in the lattice parameters of ZnO can indeed provide variations in band gaps: a decrease in a, b, or c leads to smaller band gaps along with the shift of the absorption edge to the lower energies, while the opposite trend is observed when increasing a, b or c [53].

The mesh parameter of hexagonal structure materials ($a=b\neq c$, $\alpha=\gamma=90°\neq\beta$) is connected to the indices (h,k,l) and the position of the d_{hkl} peaks by the following relation [54]:

$$d_{hkl}=\frac{1}{\sqrt{\frac{4}{3a^2}\left(h^2+k^2+hk\right)+\frac{l^2}{c^2}}} \quad (4)$$

The D values evaluated vary in the range of 15−18 nm. It is also noted that the size of the crystals increases initially with the introduction of Fe into the ZnO films and then decreases with an increase of 6 wt.% of the doping concentration while obtaining a small crystal size estimated at 15 nm. A lower value of dislocation density (δ), which is the number of dislocation lines per unit volume present in the fabricated films, indicates fewer defects in the deposited layers and the formation of higher-quality films at 6 wt.% doping concentration [55].

Lattice strain (ε) is mainly caused by the mismatch between the polycrystalline film and the glass substrate [56]. The minimum value of ε obtained for 6 wt.% Fe indicates less lattice mismatch with fewer defects between the substrate and the grown ZnO film. The additional increase in pressure at higher Fe-doping concentration can be attributed to the shift in the preferred direction. This means that the doping effect creates crystal defects and leads to charge imbalance around the doping. Moreover, it was found that the ZnO film containing 6 wt.% Fe-doping showed small crystalline size, dislocation density, and less lattice defects than other samples.

Table 2 Lattice parameters (a, b, c) of studied sample as function of Fe content

Sample	Phase	θ/(°)	(hkl)	d_{hkl} (=$n\lambda$/(2sinθ))/Å	a/Å	b/Å	c/Å
ZnO	ZnO	15.85	(100)	2.821	3.257	3.257	5.642
		17.15	(002)	2.612			
2 wt.% Fe:ZnO	ZnO	14.97	(100)	2.981	3.442	3.442	5.961
		16.07	(002)	2.783			
4 wt.% Fe:ZnO	ZnO	14.95	(100)	2.985	3.446	3.446	5.563
		16.07	(002)	2.782			
6 wt.% Fe:ZnO	ZnO	14.97	(100)	2.981	3.442	3.442	5.563
		16.07	(002)	2.782			

Therefore, Fe-doping concentration of 6 wt.% was chosen to improve the ZnO layers and obtain better structural properties and, thus, a more effective surface. According to the properties obtained, 6 wt.% Fe:ZnO sample is a highly sensitive photodetector for visible light and a good motivator in photocatalytic applications [49,51].

RAMBU et al [57] studied thin films of zinc oxide deposited by a sol−gel method. They found that the polycrystalline structure is of Wurtzite type. The doping with 6 wt.% and 8 wt.% of Fe showed a $ZnFe_2O_4$ spinel phase. It was attributed to the high concentrations of Fe, which resulted in a decrease of the (002) peak intensity. The increase in the doping ratio caused an increase in the crystal size from 196 to 255 Å [57].

YADAV et al [58] confirmed that no secondary phase appeared except for the ZnO phase (hexagonal Wurtzite) after the deposition of ZnO thin layers using the rf magnetron sputtering technique on c-Si substrates. The same behavior was observed with an increase in the concentration of iron doping with a shift of the peaks towards small angles. This is due to the formation of a triangular pyramid through the union of an oxygen atom adjacent to four Zn atoms. The oxygen is concentrated with an increase in the distance between the Zn—O and Zn—Zn bonds. The replacement of Zn^{2+} ions with an ionic radius of 0.60 Å is done with smaller Fe^{3+} ions with a radius of 0.49 Å [58].

TAHA et al [59] found that the Wurtzite structure of $Zn_{1-x}Fe_xO$ does not change, and no secondary phases or impurities were detected as a result of iron doping such as FeO, and Fe_3O_4 when the sol−gel technique was utilized to deposite the layers. This result is attributed to the incorporation of iron ions into zinc sites within the crystal lattice. The effect of iron incorporation was noticeable through an increase in the size of the granules when iron ions were replaced with zinc, as an increase in the distance between atoms caused the lattice to expand [59].

3.2 Atomic force microscopy (AFM)

Figure 4 shows the 3D morphology of Fe:ZnO thin films deposited on glass substrates with different concentrations. It can be seen that the pure Zn sample (Fig. 3(a)) has a regular topography along the surface. The roughness is lower than samples with 2 wt.% Fe:ZnO, 4 wt.% Fe:ZnO and 6 wt.% Fe:ZnO after iron doping, where the formation of irregular hierarchical grains on the surface of the samples is observed. Statistical processing of AFM images over a 3 μm area using Gwyddion software allowed us to estimate the grain

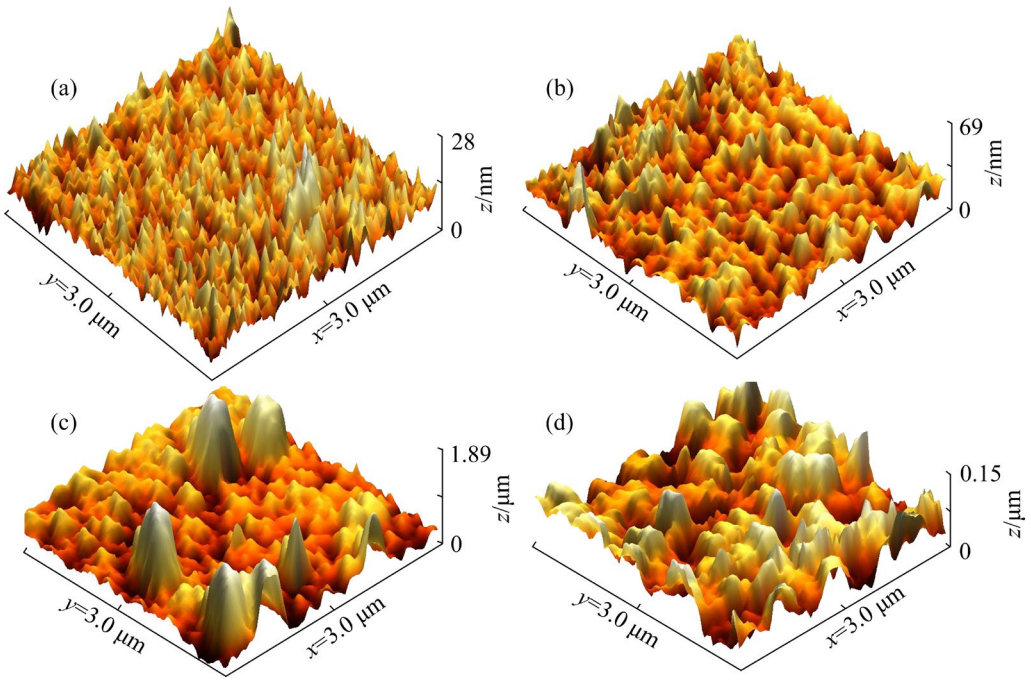

Fig. 4 AFM measurements of surface for different concentrations of Fe doping: (a) ZnO; (b) 2 wt.% Fe:ZnO; (c) 4 wt.% Fe:ZnO; (d) 6 wt.% Fe:ZnO

size variation of Fe-doped ZnO thin layers and their roughness as a function of doping concentration (Fig. 4).

These values show that the grain size increases as the iron concentration increases from 58 nm in the case of pure ZnO to 138 nm with an iron doping concentration of 6 wt.%.

On the other hand, the RMS roughness values increased to 46 nm for the 6 wt.% Fe:ZnO sample compared to 7.40 nm for a pure ZnO sample (Fig. 5). A deterioration of the surface texture is then observed with doping. The increase in size and roughness as a function of iron doping concentration from 2 to 6 wt.% Fe can be attributed to the introduction of iron as a substitute in the ZnO lattice and the appearance of the new Fe_2O_4 phases.

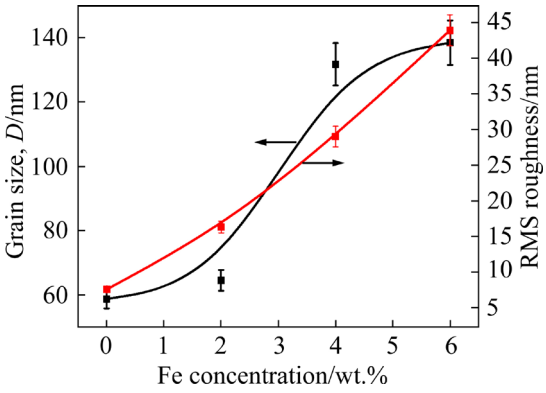

Fig. 5 Variation in grain size of Fe-doped ZnO thin films for different doping concentrations

The AFM images show self-affine surfaces (Fig. 4). The scaling behavior of the roughness is characterized by three parameters: (1) RMS value of surface heights (S_q) (vertical fluctuations of roughness), (2) the correlation length (ξ) indicating the distance on the surface over which the points can be considered uncorrelated, and (3) the roughness exponent (α) measuring the relative contribution of high-frequency fluctuation to roughness. These parameters were obtained from the height–height correlation function (HHCF), $H(r)$. The HHCF is defined by the statistical average of the mean square of height difference between the pair of points, separated by a distance (r), and is written as [60]

$$H(r)=\langle|h(r+r')-h(r')|^2\rangle \quad (5)$$

where $H(r)$ is the surface height at a point r and $H(r+r')$ at a point r shift by a quantity r'.

The HHCF function $H(r)$ can be modelized by a function [61]:

$$H'(r)=2\sigma^2\{1-\exp[-(r/\xi)^{2\alpha}]\} \quad (6)$$

where σ is the interface width, ξ is the lateral correlation length, and α is the roughness exponent. α gives the fractal characteristics of the random surface and is related to the Horsdorff dimension or fractal dimension D_f with $D_f=d-\alpha$. Here d is the embedded dimension of the surface. When $\alpha=1$, the surface is random with a Gaussian correlation.

The lg–lg plot of $H(r)$ is obtained from AFM images as a function of distance r and is shown in Fig. 6. The measured values are fitted with the modelized equation of the HHCF with the goal of extracting the parameters α. The HHCF is divided into two distinct regions as a function of r. For $r \ll \xi$, the curve is a right curve, and for $r \gg \xi$, the function reaches a plateau. The saturation values correspond to the long-range film roughness and $H'(r) \sim 2\sigma^2$.

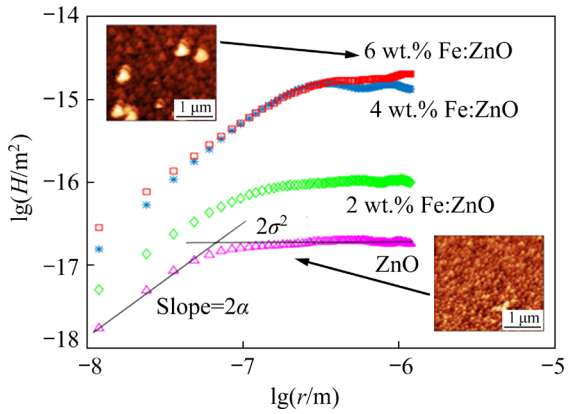

Fig. 6 lg–lg plot of HHCF, $H(r)$ as function of distance r for Fe-doped ZnO thin films on glass substrate for different doping

The values of ξ and α are plotted in Fig. 7. The correlation length has a maximum of 2 wt.% doping. It can be observed that the Hurst exponent or the roughness exponent decreased as a function of the doping. The Hurst parameter measures the short-range roughness or estimates the random fluctuations in the short range. When the doping is increased, the grain surface structure is reduced, and the height irregularities S_q are improved. For a pure ZnO material, a low value is measured. This value of α means that a large contribution of high spatial frequency fluctuations to the roughness is present in Table 3.

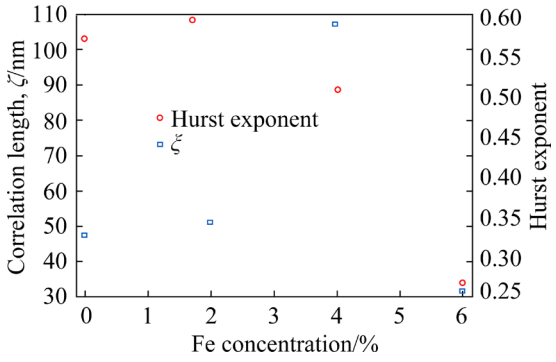

Fig. 7 Evolution of correlation length ξ and α (Hurst exponent or short-range roughness)

Table 3 Mean roughness and kurtosis of samples

Sample	Mean square roughness or RMS of height irregularities, S_q/nm	Mean roughness, S_a/nm	Kurtosis, γ_2
ZnO	3	2	1
2 wt.% Fe:ZnO	7	5	4
4 wt.% Fe:ZnO	29	23	−0.3
6 wt.% Fe:ZnO	27	17	6

RAMBU et al [57] found similar results when they evaluated the effect of iron with 6 wt.%, 8 wt.%, and 10 wt.% doping on the surface of ZnO films. They observed that the surface undergoes modifications with the formation of crystals with nano-longitudinal shapes characterized by voids and elevations in the case of pure zinc oxide. However, an increase in the percentage of doping resulted in a change in the shape and fusion of the crystals, which contributed to an increase in their size [57]. The 3D analysis with AFM [62] with doped ZnO thin films with concentrations of 2, 4, 6, and 8 wt.% Fe prepared by spin-coating technique revealed that the addition of Fe increases the surface roughness and porosity and decreases particle sizes (from 100 nm for ZnO to 72 nm for 8 wt.% Fe:ZnO) [62] contrary to our experiment.

3.3 Scanning electron microscopy (SEM)

The ZnO thin layers observed with SEM in Figs. 8(a−d) showed that they have a morphology that looks like undulated wave patterns. The results indicate that the samples have a coarse thickness. This can be attributed to the effect of the spin-coating method used to deposit a significant layer on the substrate. The technique of fabrication leads to the growth and agglomeration of the primary nuclei in the form of a uniform structure that appears as a crust. A high concentration of iron (6 wt.%) led to the appearance of irregular cracks on the surface of the sample and showed ganglia-like hills.

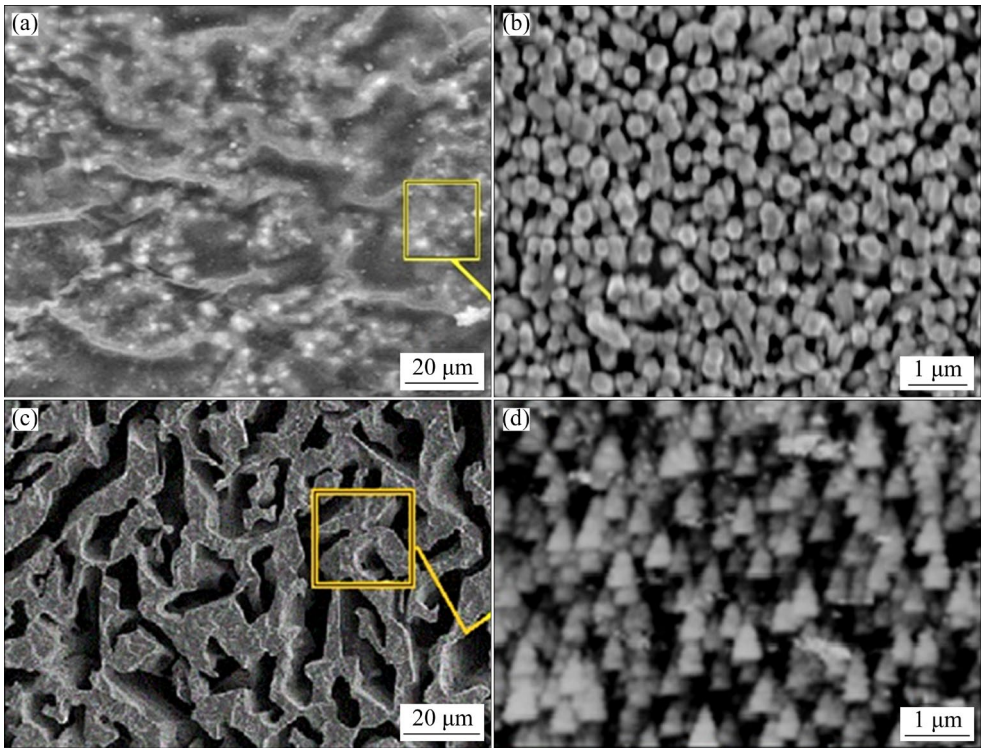

Fig. 8 SEM images of thin layers of ZnO before (a, b) and after (c, d) doping with 6 wt.% Fe

A magnified image in Figs. 8(b, d) presents the shape of the granules. A change from spherical for pure ZnO layers to a pyramid-like shape after doping with 6 wt.% Fe, which was previously demonstrated by AFM, is observed.

These results are consistent with the results of YAO et al [62]. Samples of ZnO on a glass substrate was formed at the nano-size similar shapes with a uniform structure with hills that resemble smooth knots when the image was enlarged. The 4 wt.% Fe:ZnO sample showed a wafer-like structure oriented in different random directions [62].

The SEM images of Fe-doped ZnO films prepared by SRINIVASULU et al [63] using spray pyrolysis technique showed small size grains distributed along the surface. With the increase in the concentration of iron, the surface roughness increased due to the inhomogeneous distribution of granules and the occurrence of agglomerations due to gathering of primary nuclei, which contributed to the formation of a compacted layer [63]. Surface analysis images of ZnO and Fe:ZnO samples prepared by KAFLE et al [64] show that the size of the granules increases with the concentration of steroids of 4 wt.%, through the formation of granules that take the form of long columns similar to earthworms [64].

For EDAX analysis, the spectra recorded for ZnO and ZnO doped with 6 wt.% Fe are shown in Fig. 9. It is observed that the chemical composition of zinc oxide (Fig. 9(a)) consists only of the basic constituents zinc (Zn) and oxygen (O). For Fe-doped ZnO (Fig. 9(b)), the Zn peak is well diffracted with traces of impurities in negligible proportions, which are provided by base powder. The EDX images consist of Zn, O, and Fe peaks. They confirm the presence of a Fe content of approximately 14.2 wt.% while the zinc amounted to be 46.7 wt.% in the Fe:ZnO sample, as shown in Fig. 9(b). This is consistent with the results of KAFLE et al [64], where the presence of the iron peak can be clearly seen even if the doping is weak.

3.4 Optical properties of Fe:ZnO thin layers

The optical properties of undoped and Fe-doped ZnO thin films with different concentrations (0−6 wt.%) were studied using the UV−Vis spectrophotometer in transmission mode. The UV−Vis transmittance spectra of ZnO-based thin films were acquired in the range of 200−900 nm and are presented in Fig. 10.

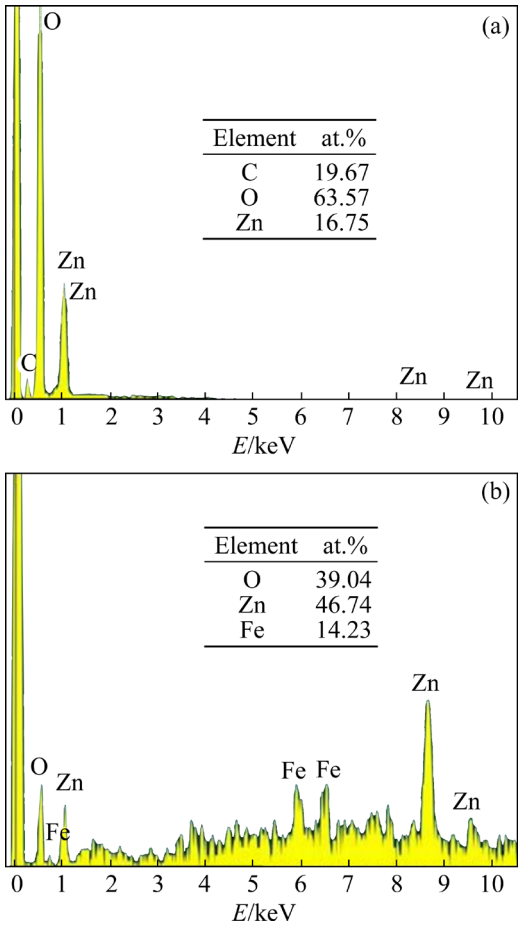

Fig. 9 EDX spectra of ZnO (a) and 6 wt.% Fe-doped ZnO (b)

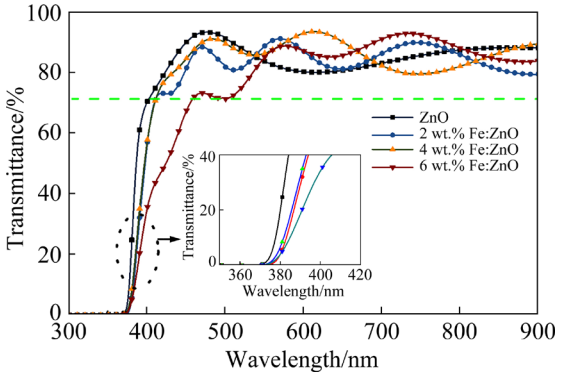

Fig. 10 Transmittance spectra of Fe-doped ZnO thin films with different concentrations (0, 2, 4, and 6 wt.%) deposited on glass substrates

As can be seen, a high transparency in the visible region of 400−800 nm is observed for all samples. The average transmittance exceeds that (T_{moy}>80%). However, the transmittance of ZnO slightly decreases up to (~75%) as the Fe

concentration increases. This effect may be due to the increase in optical scattering due to the surface morphology observed by SEM. Moreover, interference fringes were also observed due to multiple reflections at different interfaces and indicated that all deposited films are smooth, uniform, and thick [65].

On the other hand, we observed a small shift of the absorption edge towards low energies with increasing Fe concentration. This shift confirms that the Fe has been incorporated correctly into the ZnO matrix. This shift also confirms the existence of a change in the energy gap of the samples before and after doping.

RAMBU et al [57] studied the optical properties to find out the effect of iron doping deposited with spin-coated technology. It was found that the transmittance of the films decreases with an increase in the concentration (ranging between 80% and 90%). This effect is due to the formation of secondary phases and the increase in surface roughness and thickness, as well as defects in the crystal lattice. The same behavior was also observed with the increase in the percentage of iron by controlling the absorption edge in a direction towards higher wavelengths [57].

The results are also similar to those reached by KAFLE et al [64], where the transmittance of the samples deposited by the spin method was 75% for 4 wt.% Fe:ZnO film and 85% for a pure ZnO film with a shift in the spectra of the samples in the presence of an increase in the concentration of iron [64].

The UV−Vis absorption spectra (about 375 nm) give the value of the gap energy E_g with the Tauc's method, by plotting the curve $(\alpha h\nu)^2$ as a function of $h\nu$ and then by extrapolating the linear part. The intersection point of the tangent with the horizontal axis at $\alpha h\nu$=0, allows to extract the value of the gap E_g. The Tauc curves are shown in Fig. 11(a). The optical band gap of the thin films is determined by Eq. (7) [66]:

$$(\alpha h\nu)=A(h\nu - E_g)^{1/2} \quad (7)$$

where A is a constant, $h\nu$ is the photon energy, and E_g is the optical band gap.

The evolution of the ZnO optical gap as a function of the Fe doping concentration is presented in Fig. 11(b). The gap energy refers to the electronic transitions that take place at the semiconductor level. The gap energy of ZnO is 3.20 eV. This value is consistent with reported data [57]. In this figure, we see that the ZnO gap decreases from 3.20 to 3.03 eV, when the Fe concentration increases from 0 to 6 wt.%. This decrease can be attributed to the appearance of doping energy levels in the bandgap of ZnO, leading to its reduction.

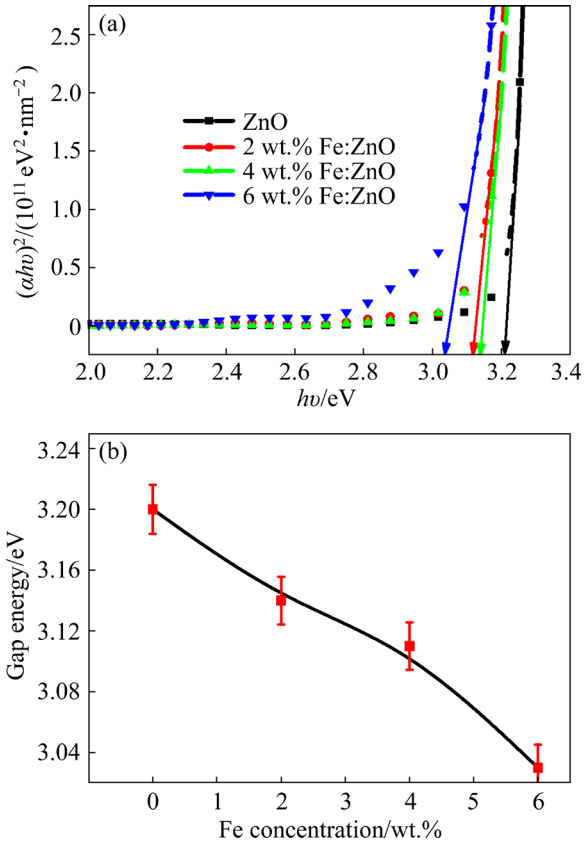

Fig. 11 Determination of gap energy by extrapolation of linear part of Tauc curve for Fe:ZnO thin layers

Changes in their band gaps and shifts in absorption edges with respect to alteration in the lattice parameter have been investigated by optical measurements. It is possible to shrink a by about 0.018 nm (or 1.8%), that leads to the gap reduction from 3.20 eV (ZnO) to 3.03 eV (6 wt.% Fe:ZnO). By means of initial calculations, we explore the possibility of manipulating band-gap values in ZnO along with the corresponding shift in the absorption edge by changing its a, b, and c lattice parameters during iron doping. It is revealed that an increase in any of the lattice parameters provides band-gap enlargement, while the opposite trend is observed when decreasing the lattice parameters [53].

Owing to the reduced optical bandgap, the results revealed that Fe-doping can lead to

significant improvement in the electrolysis activity of ZnO. The ZnO thin layers showed the optimum photocatalytic and electrolysis activity for 6 wt.% Fe doping, which was attributed to the presence of maximum dopant ions in the ZnO matrix. The enhanced photocatalytic, electrolytic, and photo-detector performance of Fe:ZnO could increase its scope of industrial and commercial applications [59,62].

The results presented are consistent with those of YAO et al [62]. They concluded in their study that the energy gap decreases with an increase of the iron content from 3.75 V, which corresponds to 0 wt.%, to 3.3 eV, which corresponds to 8 wt.%. This is due to the emergence of donor levels near the conduction band within the energy gap of zinc oxide due to the presence of banned impurities [62]. KAFLE et al [64] showed an inverse behavior. They observed a sudden increase in the energy gap from 3.25 to 3.4 eV. They attributed this difference to the polycrystalline nature of the films, the complex crystalline phases, and distortions in the crystalline structure [64].

3.5 XPS analysis

X-ray electron spectroscopy was used to estimate the chemical composition and to determine the valence state of iron in Fe:ZnO films prepared at a substrate temperature of 500 °C with a doping concentration of 6 wt.%. XPS spectra were analyzed by taking the C 1s peak (284.5 eV) as a reference. The atomic concentrations of different elements present in the films were also calculated using the areas under the respective peaks. From Fig. 12(a), it is seen that the strong peaks observed at 1021.21 and 1045 eV, respectively, correspond to Zn $2p_{3/2}$ and Zn $2p_{1/2}$. However, full scans of pure ZnO films doped with iron showed high resolution spectra for the constituents shown in Fig. 12(b).

The variations of peak intensities of oxygen and iron in 6 wt.% Fe-doped ZnO films are shown in Figs. 13(a, b). The peaks observed at 713.12 and 729.13 eV with a peak separation of 16.41 eV were different from the binding energy values of Fe and Fe in FeO and are, therefore, due to the Fe $2p_{3/2}$ and Fe $2p_{1/2}$ peaks, respectively (Fig. 13(a)) [51]. This confirms the presence of iron in the 3+ state in the

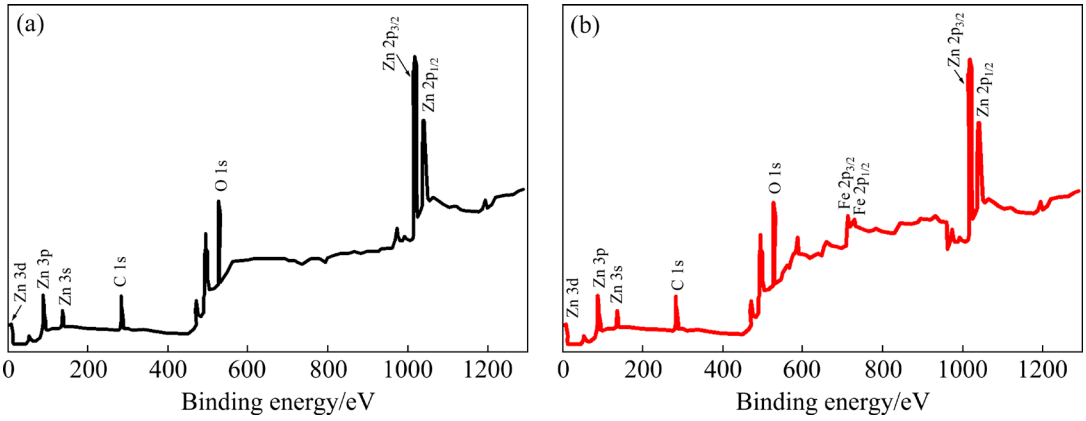

Fig. 12 XPS spectra of ZnO (a) and Fe-doped ZnO (b) thin layers

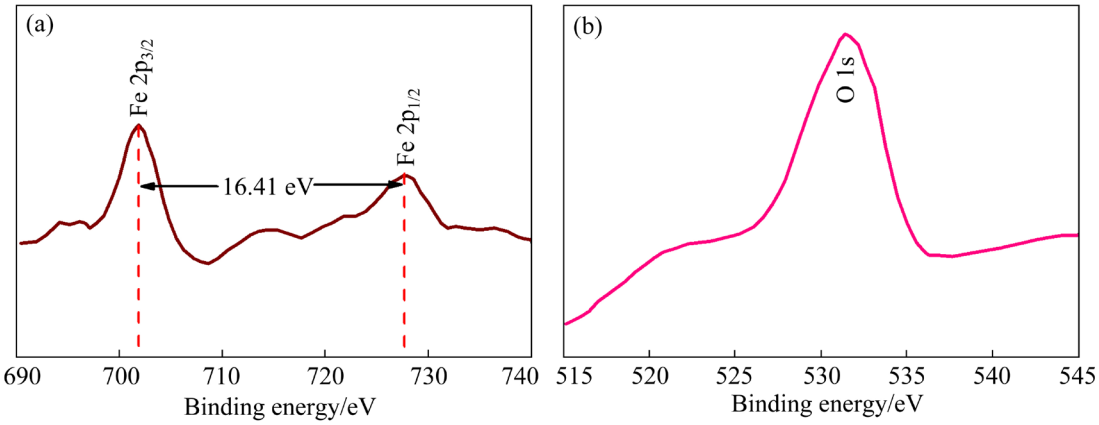

Fig. 13 Narrow scan XPS spectra of Fe 2p (a) and O 1s (b) peaks of 6 wt.% Fe-doped ZnO layers

experimental films. The binding energy peaks obtained for Fe^{3+} agree closely with the peaks (713.12 eV of Fe $2p_{3/2}$ and 729.13 eV of Fe $2p_{1/2}$) for Fe^{3+} mentioned in the Handbook of X-ray photoelectron spectroscopy [52]. It can also be observed that the O 1s region is confirmed with a peak at 531.2 eV (Fig. 13(b)), and this can be attributed to O^{2-} ions in the Wurtzite structure of hexagonal ZnO [57,58]. The broad nature of the peak could be due to the different coordinations of oxygen in the films.

These results agree with the results of RAMBU et al [57], where the XPS analysis of the samples (ZnO, 6 wt.% Fe:ZnO, 8 wt.% Fe:ZnO and 10 wt.% Fe:ZnO) indicated that Zn^{2+} ions are replaced by both Fe^{3+} and Fe^{2+} ions, due to the different temperatures that were used during the treatment. Also obtained values are close to what was obtained for the binding energy peaks at 711.13 and 724.66 eV, which respectively correspond to Fe $2p_{3/2}$ and Fe $2p_{1/2}$ bound to Fe^{3+} ions in Fe-doped ZnO films prepared by spin coating technique [59].

The $ZnFe_2O_4$ phase changes the surface shape with the difference in the doping ratio. SRINIVASULU et al [63] found that the binding energies of ZnO samples prepared with a Fe-doping of 6 wt.% and 1 wt.% were close to the standard binding energies of Zn in zinc oxide and differed from the initial binding energies. This result confirms its presence in the films [63].

3.6 Sensitivity of thin layers for photodetectors in dark/UV light

Photodetectors consist of a homogeneous (photosensitive) semiconductor material that is connected to an electrical circuit by means of two electrodes. A voltage difference between the two different electrodes is applied to delivering a current. Under the influence of the light beam, the photodetector generates electron−hole pairs that modulate the conductivity of the absorbed layer and, thus, the conductivity of the semiconductor. An increase in the current intensity in the circuit will occur.

Electrical measurements were performed in order to test the light sensitivity of the Fe:ZnO thin films. The electrical properties of the voltage were measured in the dark and under UV illumination (λ=254 nm) by changing the applied voltage in the range of 0−12 V and by acquiring the value of the current flowing through the sample.

Based on the measurements, it can be observed that the photocurrent and the dark current increase respectively as a function of the applied bias voltage due to the increase in the velocity of the charge carriers (Fig. 14) [67,68]. Moreover, the curves show a linear variation. The slope of these linear segments represents the ohmic resistance of the materials according to Ohm's law $U=RI$, which means that ZnO-based photodetectors have an ohmic behavior. This linearity is a very important parameter for photodetectors. The sensitivity can be maximized when the metal-semiconductor junction is ohmic [69].

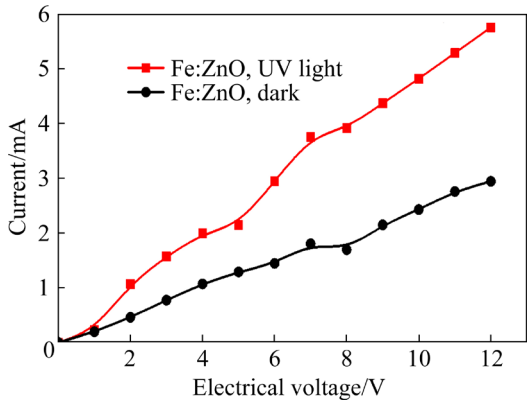

Fig. 14 Photodetector measurements of Fe:ZnO thin layers in dark and under UV illumination

Moreover, the behavior of the ultra-linear photocurrent also indicates that some carriers are directly injected into the conduction band of Fe:ZnO of a metal electrode [70]. Importantly, the photocurrent of the photodetectors is larger than the dark current, and this effect shows that Fe:ZnO-type samples have significant photosensitivity to UV light. As can be seen in Fig. 14, the photocurrent values I_{ph} measured for 6 wt.% Fe:ZnO at 12 V bias are 5.73 mA and 2.95 mA for I_{dark}.

In Fig. 15, under darkness, oxygen molecules (O_2(g)) are adsorbed on the surface of the films and trap free electrons, thus forming a depletion zone on the surface of Fe:ZnO (Fig. 15(b)) [71]:

$$O_2(g)+e \rightarrow O_2^- \quad (8)$$

The formation of a large number of ionized oxygen on the surface of thin films leads to the formation of a charge depletion zone near the surface, resulting in the separation of charge

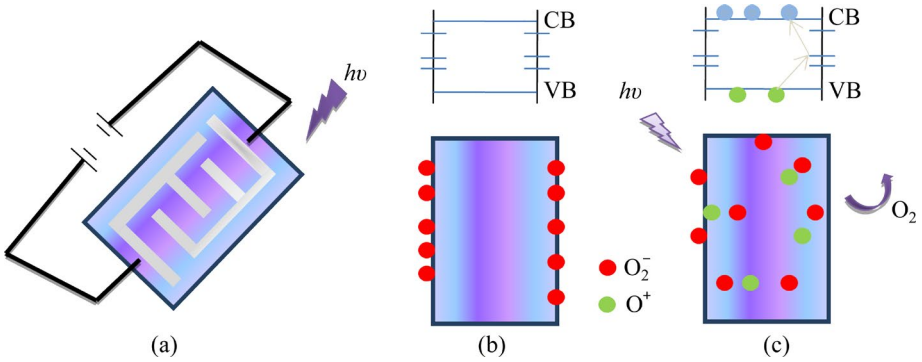

Fig. 15 Schematic representation of photoconduction phenomenon in photo-detector under UV illumination (a); State of films and energy band diagram under darkness (b); State of layers and energy band diagram under illumination, with phenomena of oxygen desorption (c)

carriers and minimizing their recombination. The illumination of the sample with photons whose energy is greater than the energy band gap of 3.03 eV (i.e., in the UV range) induces the generation of electron−hole pairs (Eq. (9)). The potential gradient created by the depletion zone at the surface activates the diffusion of holes towards the surface which cause the desorption of adsorbed oxygen molecules O_2^-(ads) (Fig. 15(c)).

$$Fe:ZnO+h\nu \rightarrow e+h^+ \quad (9)$$

$$h^++O_2^- \rightarrow O_2(g) \quad (10)$$

The remaining unpaired electrons can then be collected by applying a voltage to the terminals of the nanofilms, whose conductivity is thus increased. The current dynamics measured in the layers under illumination for different application voltages are shown in Fig. 15. Photo-conductivity mechanism involving the adsorption and desorption of oxygen molecules remains effective even on very short time scales (1 ns) [72].

With this type of photo-detectors [73], high photo-conductive gains with high sensitivity are obtained. However, this high photoconductivity requires significant operating voltages, up to 12 V, and, therefore, a significant external energy input. Furthermore, the high intensity of the involved electric fields is responsible for local disturbances in the depletion zone, leading to increased rise and fall times [74].

In a previous study, KURNIAWAN and RAHMI [75] manufactured tin oxide nanoparticles based on electrolysis using a tin plate. The process was carried out in 100 mL of the electrolyte solution, and by applying a variable voltage from 10 to 100 V, the formation of SnO_2 particles was monitored. After 15 min, the electrolysis was stopped, and bubbles were released at the cathode, indicating the production of hydrogen gas. At the same time, Sn was oxidized to Sn^{2+} or Sn^{4+} ions at the anode [75].

3.7 Electrolysis of thin layers

Electrolysis is a process in which an electric current, using a direct current source, is transmitted through a liquid or solution containing ions and results in a disintegration of substances. The cations and anions that make the salts are agitated when they are dissolved in water and are attracted to the cathode, which is the pole of the electrochemical cell at which reduction occurs, or at the anode, which represents the pole of the electrochemical cell at which oxidation occurs.

With the goal of finding out the effect of iron doping on the properties of zinc oxide in the decomposition of the organic compound methylene blue, we made electrical contacts with silver at the level of the two samples (ZnO and 6 wt.% Fe:ZnO) and then covered this contact with insulating layers. A voltage of 10 V was applied each time for 1 h. The experimental setup is shown in Fig. 16.

According to Fig. 16(a), it is possible to observe the appearance of black color on the surface of the two samples, followed by a noticeable decrease in the transmittance of the two samples. A reduction in the absorbance and concentration of the methylene blue solution during the electrolysis process (Fig. 16(b)) is simultaneously observed. In the case of iron-doped zinc oxide, the dissociation is more efficient

compared to pure zinc oxide. This effect can be explained by the quality and effectiveness of the surface, which is characterized by the presence of a greater number of ions (Zn^{2+} and Fe^{2+}) that disintegrate the dye and release carbon dioxide (CO_2) and H_2O (Fig. 17).

A digital multimeter is used to measure the potential between the two ends of the thin-layered sample of Fe-doped zinc oxide. Figure 16(b) shows a response of the sample through the measured voltage value, which was estimated at a value of 19.8 V.

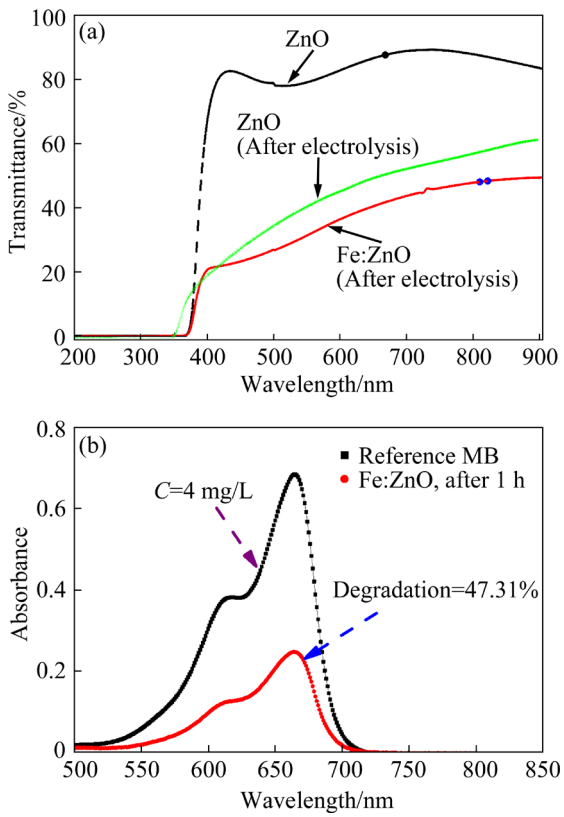

Fig. 16 Transmittance spectra of pure ZnO and Fe:ZnO before and after electrolysis of methylene blue (a) and absorbance spectra showing degradation of MB by Fe:ZnO (b)

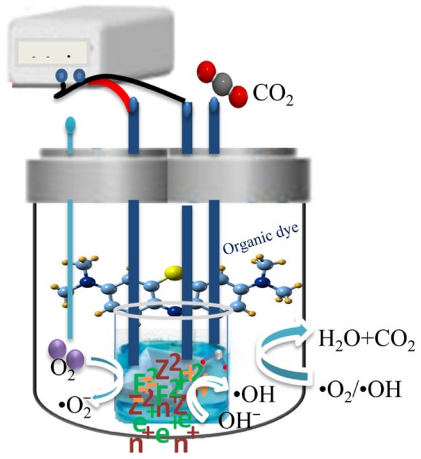

Fig. 17 Electrolysis phenomenon of thin layer under visible light

Figure 17 shows how the organic dye methylene blue oxidizes and decomposes into carbon dioxide (CO_2) and water (H_2O) based on the application of an electric current in the sample Fe:ZnO. The experiment results in the creation of a reaction of holes (h^+) with water (H_2O) to produce hydroxide ·OH, which contributes to the decomposition of the colored substance [76] and the interaction of free electrons (e) with oxygen (O_2) to give the white color to the polluted solution (Eqs. (11)−(15)) [77].

When an electric current is applied between the two ends of the sample, the positive side of the generator repels the gaps from it, so it rushes and flows into the sample, while the negative side of the generator repels electrons from it and rushes from it into the opposite side of the same film. Since the chamber contains oxygen, the free electrons on the surface of the sample pick up O_2 to form $\cdot O_2^-$ (Eq. (13)) [76,77].

Both the electrical intensity and the sufficient energy absorption of visible light applied to the sample contribute to the occurrence of disturbances in the depletion region, which led to a reduction in them and the passage of electric current. On the other hand, the electrical intensity enabled the creation of (e^-/h^+) pairs in zinc oxide (Eq. (15)) and prevented re-combination through iron inoculation (Eq. (12)), which also worked to increase the electrons formed in the conduction band (CB) [70]. The holes (h^+) present in the valence band (VB) of zinc oxide also react with water to produce a number of ·OH radicals (Eq. (14)) [71]. The mentioned interactions are summarized in the following equations:

$$Fe{:}ZnO + \text{visible light} \rightarrow e + h^+ \quad (11)$$

$$Fe \rightarrow Fe^{2+} + 2e \quad (12)$$

$$Fe{:}ZnO(e) + O_2 \rightarrow \cdot O_2^- \quad (13)$$

$$Fe{:}ZnO(h^+) + OH^- + H_2O \rightarrow \cdot OH \quad (14)$$

$$\cdot OH + \cdot O_2^- + h^+_{VB} + \text{degraded dye} \rightarrow CO_2\uparrow + H_2O \quad (15)$$

BOURAS et al [78] used pure zinc oxide films doped with 2% and 4% of silver, deposited on a silicon substrate by spin-coating technique, in the goal to study their uses as photodetectors of

ultraviolet radiation. It was found that under the influence of darkness, the saturation current was extracted, which is 4 times and 12 times less in the case of doping with 2% and 4%, respectively [78,79]. Under the influence of ultraviolet radiation at λ=254 nm, a non-linear relationship was extracted between the voltage and the response, which confirms that the fabricated devices respond with a Schottky behavior [80,81].

The study made it possible to know that the silver-doped films had a higher detection rate compared with the pure zinc oxide films due to an increase in the surface roughness [82−84]. Thin-doped samples provide better performances and are effective by increasing the concentration of silver. They are accompanied by a noticeable increase in sensitivity, which reached 3.3×10^{-9} W for ZnO and 4.44×10^{-10} W for 4% Ag:SZO [78,79].

4 Conclusions

(1) The effect of the doping ratio of Fe of the layers was studied by measuring the morphological, optical, and structural properties.

(2) The morphological analysis showed that the surface roughness values of the ZnO layers deposited on the glass substrates vary between 8 and 45 nm.

(3) The optical transmittance was in the range of 87%−91% in the UV−Vis region.

(4) A decrease in the values of E_g was obtained when the content of iron increased.

(5) It is observed that all the layers obtained are polycrystallines with a structure hexagonal with Wurtzite type.

(6) Photodetectors based on Fe-doped ZnO exhibits considerable photosensitivity to ultra-violet radiation.

(7) Effective degradation of methylene blue organic compound by Fe:ZnO thin film electrolysis occurs.

CRediT authorship contribution statement

Dikra BOURAS: Writing − Original draft preparation, Visualization, Resources; **Mamoun FELLAH:** Supervision, Data curation, Writing − Original draft preparation, Conceptualization, Methodology, Software, Writing − Reviewing and editing, Project administration; **Régis BARILLÉ:** Writing − Reviewing and editing; **Amjad IQBAL:** Methodology, Software, Reviewing; **Hamadi FOUZIA:** Original draft; **Obrosove ALEKSEI:** Original draft, Resources; **Gamal A. EL-HITI:** Writing − Reviewing and editing.

Declaration of competing interest

The authors declare that they have no known competing financial interests or personal relationships that could have appeared to influence the work reported in this paper.

Acknowledgments

The Laboratory of MOLTECH-Anjou, Angers University, France, has supported this work. The authors acknowledge the support received from the Researchers Supporting Project (No. RSP2024R404), King Saud University, Riyadh, Saudi Arabia.

References

[1] RAHA S, AHMARUZZAMAN M. ZnO nanostructured materials and their potential applications: Progress, challenges and perspectives [J]. Nanoscale Advances, 2022, 4: 1868−1925.

[2] BOURAS D, MECIF A, BARILLÉ R, HARABI A, RASHEED M, MAHDJOUB A, ZAABAT M. Cu:ZnO deposited on porous ceramic substrates by a simple thermal method for photocatalytic application [J]. Ceramics International, 2018, 44(17): 21546−21555.

[3] DU Si-chao, YIN Ju-xin, XIE Hao, SUN Yun-lei, FANG Tao, WANG Yu, LI Jing, XIAO Duo, YANG Xiao-guang, ZHANG Shuo, WANG Da-wei, CHEN Wen-chao, YIN Wen-yan, ZHENG Rong-kun. Auger scattering dynamic of photo-excited hot carriers in nano-graphite film [J]. Applied Physics Letters, 2022, 121(18): 181104.

[4] HUANG Bo-long. Doping of RE ions in the 2D ZnO layered system to achieve low-dimensional upconverted persistent luminescence based on asymmetric doping in ZnO systems [J]. Physical Chemistry Chemical Physics, 2017, 19: 12683−12711.

[5] BOURAS D, RASHEED M. Comparison between CrZO and AlZO thin layers and the effect of doping on the lattice properties of zinc oxide [J]. Optical and Quantum Electronics, 2022, 54: 824.

[6] PINO P, BOSCO F, MOLLEA C, ONIDA B. Antimicrobial nano-zinc oxide biocomposites for wound healing applications: A review [J]. Pharmaceutics, 2023, 15(3): 970.

[7] AKHMEDOV A, ABDUEV A, MURLIEV E, ASVAROV A, MUSLIMOV A, KANEVSKY V. The ZnO−In_2O_3 oxide system as a material for low-temperature deposition of transparent electrodes [J]. Materials (Basel), 2021, 14(22): 6859.

[8] ZEIDAN M M, ABEDRABBO S. Neutron irradiation to transmute zinc into gallium [J]. Nanomaterials (Basel), 2023, 13(9): 1487.

[9] STAMBOULI I, ZEROUALI M, DAÏRA R, BOURAS D,

EL-HITI G A, GRIGORIAN S, FELLAH M. Enhancement of tin-doping on the structural, electrical, and optical properties of copper oxide thin films for optoelectronic applications [J]. Ceramics International, 2025. https://doi.org/10.1016/j.ceramint.2025.01.540

[10] ZHAO Chen-yang, CHEUNG Chi-fai, XU Peng. High-efficiency sub-microscale uncertainty measurement method using pattern recognition [J]. ISA Transactions, 2020, 101: 503−514.

[11] FELLAH M, ABDUL SAMAD M, LABAÏZ M ASSALA O, IOST A. Sliding friction and wear performance of the nano-bioceramic α-Al_2O_3 prepared by high energy milling [J]. Tribology International, 2015, 91: 151−159.

[12] GOKTAS A, MUTLU I.H, YAMADA Y. Influence of Fe-doping on the structural, optical, and magnetic properties of ZnO thin films prepared by sol−gel method [J]. Superlattices and Microstructures, 2013, 57:139−149.

[13] BADAWI A, ALTHOBAITI M G, ALI E E, ALHARTHI S, ALHARBI A N. A comparative study of the structural and optical properties of transition metals (M= Fe, Co, Mn, Ni) doped ZnO films deposited by spray-pyrolysis technique for optoelectronic applications [J]. Optical Materials, 2022, 124: 112055.

[14] WANG Y Q, YUAN S L, LIU L, LI P, LAN X X, TIAN Z M, HE J H, YIN S Y. Ferromagnetism in Fe-doped ZnO bulk samples [J]. Journal of Magnetism and Magnetic Materials, 2008, 320(8): 1423−1426

[15] SRIVASTAVA A, KUMAR N, KHARE S. Enhancement in UV emission and band gap by Fe doping in ZnO thin films [J]. Opto-Electronics Review, 2014, 22: 68−76.

[16] HAN Cong, DUAN Li-bing, ZHAO Xiao-ru, HU Zhong-min, NIU Yan-fen, GENG Wang-chang. Effect of Fe doping on structural and optical properties of ZnO films and nanorods [J]. Journal of Alloys and Compounds, 2019, 770: 854−863.

[17] GOKTAS S, GOKTAS A. A comparative study on recent progress in efficient ZnO based nanocomposite and heterojunction photocatalysts: A review [J]. Journal of Alloys and Compounds, 2021, 863: 158734.

[18] PRUSTY S, SANYAL S K, SATAPATHY J K. A contribution to the compensation of extra high voltage transmission lines [J]. Electric Power Systems Research, 1987, 12: 113−123.

[19] ANDHARE D D, PATADE S R, KOUNSALYE J S, JADHAV K M. Effect of Zn doping on structural, magnetic and optical properties of cobalt ferrite nanoparticles synthesized via Co-precipitation method [J]. Physica B: Physics of Condensed Matter, 2020, 583: 412051.

[20] SARICA E, BILGIN V. Structural, optical, electrical and magnetic studies of ultrasonically sprayed ZnO thin films doped with vanadium [J]. Surface and Coatings Technology, 2016, 286: 1−8.

[21] VIRDIAN A, MUHAMMADY S, NARADIPA M A, WIDITA R, RUSYDI A, DARMA Y. Enhancing photon absorption and conductivity of ZnO film by Fe doping: Experimental and first-principle perspectives [J]. Ceramics International, 2020, 46: 27110−27118.

[22] WANG Chang-zheng, CHEN Zhong, CHEN Zhong, HE Ying, LI Lan-ying, ZHANG Dong. Structure, morphology and properties of Fe-doped ZnO films prepared by facing-target magnetron sputtering system [J]. Applied Surface Science, 2009, 255(15): 6881−6887.

[23] DIKRA B, FELLAH M, BARILLE R, WEIß S, ABDUL SAMAD M, ALBURAIKAN A, ABD EL-WAHED KHALIFA H, OBROSOV A. Improvement of photocatalytic performance and sensitive ultraviolet photodetectors using AC-ZnO/ ZC-Ag_2O/AZ-CuO multilayers nanocomposite prepared by spin coating method [J]. Journal of Science: Advanced Materials and Devices, 2023, 9(1): 100642.

[24] BOURAS D, MECIF A, MAHDJOUB A, HARABI A, ZAABAT M, BENZITOUNI S, REGIS B**.** Photocatalytic degradation of Orange II by active layers of Cu-doped ZnO deposited on porous ceramic substrates [J]. Journal of Ovonic Research, 2017, 13: 271−281.

[25] OKE J A, JEN T C. Atomic layer deposition and other thin film deposition techniques: From principles to film properties [J]. Journal of Materials Research and Technology, 2022, 21: 2481−2514.

[26] GEREMEW T. Thin film deposition and characterization techniques [J]. Journal of 3D Printing and Applications, 2022, 1(2): 1−24.

[27] GUO Hao, XU Yong-gang, CHEN He-tuo, WANG Zheng-juan, MAO Xiao-jian, ZHOU Guo-hong, ZHANG Jian, WANG Shi-wei. Synthesis of multiwall boron nitride (BN) nanotubes by a PVD method based on vapor–liquid–solid growth [J]. Materials, 2020, 13(4): 915.

[28] FARAH M, FELLAH M, BOURAS D, HEZIL N, BECHERI A, BARILLE R, HENDA D, MONTAGNE A, TMADER A, ABD EL-WAHED KHALIFA H. Unraveling the role of sintering temperature on physical, structural and tribological characteristics of ball milled Co28Cr6Mo biomaterial based alloy [J]. Journal of Engineering Research, 2024, 12(3): 571−579.

[29] JAVED A H, SHAHZAD N, ABDULLAH KHAN M, MUNIBA A, IQBAL N, HASSAN M, NAVEED H, RAMEEL M I, SHAHZAD M I. Effect of ZnO nanostructures on the performance of dye sensitized solar cells [J]. Solar Energy, 2021, 230: 492−500.

[30] FELLAH M, HEZIL N, BOURAS D, MONTAGNE A, OBROSOV A, JAMSHED W, IBRAHIM R W, IQBAL A, EL DIN S M. ABD EL-WAHED KHALIFA H. Investigating the effect of milling time on structural, mechanical and tribological properties of a nanostructured hiped alpha alumina for biomaterial applications [J]. Arabian Journal of Chemistry, 2023, 16(17): 105112.

[31] FELLAH M, BOUCHAREB N, HEZIL N, MERAH N, ALASHKAR Y, IMRAN M, ALEKSEI O, WEISS S. Electrochemical analysis of mechanically alloyed Ti50%−Ni50% alloy for bone implants use [J]. Journal of Alloys and Compounds, 2025, 1010: 178046. https://doi.org/10.1016/j.jallcom.2024.178046

[32] WIBOWO A, MARSUDI M A, AMAL M I, ANANDA M B, STEPHANIE R, ARDY H, DIGUNA L J. ZnO nanostructured materials for emerging solar cell applications [J]. RSC Advances, 2020, 10(70): 42838−42859.

[33] QIU Chu-feng, WU Yan, SONG Jia-xing, WANG Wen-tao, LI Zai-fang. Efficient planar perovskite solar cells with ZnO electron transport layer [J]. Coatings, 2022, 12: 1981.

[34] PATIL P, SANGALE S S, KWON S N, NA S I. Innovative

approaches to semi-transparent perovskite solar cells [J]. Nanomaterials, 2023, 13(6): 1084.

[35] LIU Li-qing, WANG Hui, WANG De-hao, LI Yong-tao, HE Xue-min, ZHANG Hong-guang, SHEN Jian-ping. ZnO@TiO_2 core/shell nanowire arrays with different thickness of TiO_2 shell for dye-sensitized solar cells [J]. Crystals, 2020, 10(4): 325.

[36] WEN Zhen, FU Jing-jing, FU Jing-jing, HAN Lei, LIU Yi-na, PENG Ming-fa, ZHENG Li, ZHU Yu-yan, SUN Xu-hui, ZI Yun-long. Toward self-powered photodetection enabled by triboelectric nanogenerators [J]. Materials Chemistry C, 2018, 6(44): 11893−11902.

[37] WANG Yi-tong, XIE Wan-li, PENG Wen-bo, LI Fang-pei, HE Yong-ning. Fundamentals and applications of ZnO-nanowire-based piezotronics and piezo-phototronics [J]. Micromachines, 2023, 14(1): 47.

[38] KHANDELWAL G, DESWAL S, DAHIYA R. Triboelectric nanogenerators as power sources for chemical sensors and biosensors [J]. ACS Omega, 2022, 7(49): 44573−44590.

[39] RAHMAN F. Zinc oxide light-emitting diodes: A review [J]. Optical Engineering, 2019, 58(1): 010901.

[40] PARK S Y, KIM B J, KIM K, KANG M S, LIM K H, LEE T I, MYOUNG J M, BAIK H K, CHO J H, KIM Y S. Low-temperature, solution-processed and alkali metal doped ZnO for high-performance thin-film transistors [J]. Advanced Materials, 2012, 24(6): 834−838.

[41] DITSHEGO N M J. ZnO nanowire field effect transistor for biosensing: A review [J]. Journal of Nano Research, 2020, 60: 94−112.

[42] ALTHUMAIRI N A, BAIG I, KAYED T S, MEKKI A, LUSSON A, SALLET V, MAJID A, FOUZRI A. Characterization of Eu doped ZnO micropods prepared by chemical bath deposition on p-Si substrate [J]. Vacuum, 2022, 198: 110874.

[43] GÖKTAŞ S, ŞAHIN G. Methylene blue concentration and pH-induced photocatalytic degradation of methylene blue without photocatalyst under visible light [J]. International Journal of Advanced Natural Sciences and Engineering Researches, 2023, 7(6): 176−181.

[44] ZEROUALI M, DAIRA R, BOURAS D, BOUDJEMA B, RÉGIS B. Photocatalytic degradation of Orange II by active layers of Ag-doped CuO deposited by spin-coating method [J]. Journal of Nano Research, 2023, 80: 1−19.

[45] DAS S, GHOSH S, MISRA A J, TAMHANKAR A J, MISHRA A, LUNDBORG C S, TRIPATHY S K. Sunlight assisted photocatalytic degradation of ciprofloxacin in water using Fe doped ZnO nanoparticles for potential public health applications [J]. International Journal of Environmental Research and Public Health, 2018, 15(11): 2440.

[46] RADHA B, RATHI R, LALITHAMBIKA K. C, THAYUMANAVAN A, RAVICHANDRAN K, SRIRAM S. Effect of Fe doping on the photocatalytic activity of ZnO nanoparticles: Experimental and theoretical investigations [J]. Journal of Materials Science: Materials in Electronics, 2018, 29(16): 13474−13482.

[47] ILMETOV R. Photocatalytic activity of hematite nanoparticles prepared by sol−gel method [J]. Materials Today: Proceedings, 2019, 6: 11−14.

[48] GOKTAS S, TUMBUL A, GÖKTAŞ A. Growth technique-induced highly C-axis-oriented ZnO:Mn, ZnO:Fe and ZnO:Co thin films: A comparison of nanostructure, surface morphology, optical band gap, and room temperature ferromagnetism [J]. Journal of Superconductivity and Novel Magnetism, 2023, 36: 1875−1892.

[49] LIU Liu, LIU Zhi-wei, YANG Yi-xin, GENG Ming-qian, ZOU Yi-ming, SHAHZAD M B, DAI Yu-xiang, QI Yang. Photocatalytic properties of Fe-doped ZnO electrospun nanofibers [J]. Ceramics International, 2018, 44(16): 19998−20005.

[50] BOURAS D, MECIF A, HARABI A, BARILLÉ R, MAHDJOUB A H, ZAABAT M. Economic and ultrafast photocatalytic degradation of Orange II using ceramic powders [J]. Catalysts, 2021, 11(6): 733.

[51] KUMAR K, CHITKARA M, SANDHU I S, MEHTA D, KUMAR S. Photocatalytic, optical and magnetic properties of Fe-doped ZnO nanoparticles prepared by chemical route [J]. Journal of Alloys and Compounds, 2014, 588(5): 681−689.

[52] ASLAN F, ARSLAN F, TUMBUL A, GOKTAS A. Synthesis and characterization of solution processed p-SnS and n-SnS_2 thin films: Effect of starting chemicals [J]. Optical Materials, 2022, 127: 112270.

[53] SHOHONOV D A, MIGAS D B, FILONOV A B, BORISENKO V E, TAKABE R, SUEMASU T. Effects of lattice parameter manipulations on electronic and optical properties of $BaSi_2$ [J]. Thin Solid Films, 2019, 686: 137436.

[54] MIKAILZADE F, ÖNAL F, MAKSUTOGLU M, ZARBALI M, GÖKTAŞ A. Structure and magnetization of polycrystalline $La_{0.66}Ca_{0.33}MnO_3$ and $La_{0.66}Ba_{0.33}MnO_3$ films prepared using sol−gel technique [J]. Superconductivity and Novel Magnetism, 2018, 31(12): 4141−4145.

[55] GÖKTAŞ A, ASLAN E, ARSLAN F, KILIC A. Characterization of multifunctional solution-processed $Sn_{1-x}Zn_xS$ nanostructured thin films for photosensitivity and photocatalytic applications [J]. Optical Materials, 2022, 133(2): 112984.

[56] ASLAN E, SAHIN G, GOKTAS A. Facile synthesis of Sb_2S_3 micro-materials for highly sensitive visible light photodetectors and photocatalytic applications [J]. Materials Chemistry and Physics, 2023, 307: 128160.

[57] RAMBU A P, NICA V, DOBROMIR M. Influence of Fe-doping on the optical and electrical properties of ZnO films [J]. Superlattices and Microstructures, 2013, 59: 87−96.

[58] YADAV A K, HAQUE S M, TRIPATHI S, SHUKLA D, AHMED M A, PHASE D M, BANDYOPADHYAY S, JHA S N, BHATTACHARYYA D. Investigation of Fe doped ZnO thin films by X-ray absorption spectroscopy [J]. RSC Advances, 2016, 6: 74982−74990.

[59] TAHA T A, AHMED E M, EL-TANTAWY A I, AZAB A A. Investigation of the iron doping on the structural, optical, and magnetic properties of Fe-doped ZnO nanoparticles synthesized by sol−gel method [J]. Journal of Materials Science: Materials in Electronics, 2022, 33: 6368−6379.

[60] BOURAS D, MECIF A, BARILLE R, HARABI A, ZAABAT M. Porosity properties of porous ceramic substrates added with zinc and magnesium material [J]. Ceramics International, 2020, 46(13): 20838−20846.

[61] PATTIPAKA S, DOBBIDI P, GOUD J P, RAJU J, PRADHAN G, SRIDHAR V. Investigation of surface scaling, optical and microwave dielectric studies of $Bi_{0.5}Na_{0.5}TiO_3$ thin films [J]. Journal of Materials Science: Materials in Electronics, 2022, 33: 8893−8905.

[62] YAO Zou, ZHONG Mian, LI Shi-chen, QING Ze-hao, XING Xiao-qing, GONG Guo-chong, YAN Ran, QIN Wen-feng, SHEN Jia-qing, ZHANG Hua-zhong, JIANG Yong, WANG Zhen-hua, ZHOU Chao. Flexible wearable strain sensors based on laser-induced graphene for monitoring human physiological signals [J]. Polymers, 2023, 15(17): 3553.

[63] SRINIVASULU T, SARITHA K, RAMAKRISHNA REDDY K.T. Synthesis and characterization of Fe-doped ZnO thin films deposited by chemical spray pyrolysis [J]. Modern Electronic Materials, 2017, 3: 76−85.

[64] KAFLE B P, ACHARYA S, THAPA S, POUDEL S. Structural and optical properties of Fe-doped ZnO transparent thin films [J]. Ceramics International, 2016, 42: 1133−1139.

[65] MENG Bo, WANG Jin-long, CHEN Ming-hui, ZHU Sheng-long, WANG Fu-hui. Study on the oxidation behavior of a novel thermal barrier coating system using the nanocrystalline coating as bonding coating on the single-crystal superalloy [J]. Corrosion Science, 2023, 225: 111591.

[66] DAS S, SINHA S, DAS B, JAYABALAN R, SUAR M, MISHRA A, TAMHANKAR A J, LUNDBORG C S, TRIPATHY S K. Disinfection of multidrug resistant *Escherichia coli* by solar-photocatalysis using Fe-doped ZnO nanoparticles [J]. Scientific Reports, 2017, 7: 104.

[67] KAYANI Z N, YASEEN N, RIAZ S, NASEEM S. Investigation of Fe doping on the magnetic and optical properties of ZnO thin films [J]. Materials Research Express, 2018, 5: 036418.

[68] YOON Y J, PARK K S, HEO J H, PARK J G, NAHMB S, JIN C K. Synthesis of $Zn_XCd_{1-X}Se$ ($0\leq X\leq 1$) alloyed nanowires for variable-wavelength photodetectors [J]. Journal of Materials Chemistry, 2010, 20: 2386−2390.

[69] DING Hua-ping, GONG Pan, CHEN Wen, PENG Zhen, BU Heng-tong, ZHANG Mao, TANG Xue-feng, JIN Jun-song, DENG Lei, XIE Guo-qiang, WANG Xin-yun, YAO Ke-fu, SCHROERS J. Achieving strength-ductility synergy in metallic glasses via electric current-enhanced structural fluctuations [J]. International Journal of Plasticity, 2023, 169: 103711.

[70] HEINHOLD R, NEIMAN A, KENNEDY J V, MARKWITZ A, REEVES R J, ALLEN M W. Hydrogen-related excitons and their excited-state transitions in ZnO [J]. Physical Review B, 2017, 95: 054120.

[71] LEE C C, BIRING S, REN S J, LI Y Z, LI M Z, AL AMIN N R, LIU S W. Reduction of dark current density in organic ultraviolet photodetector by utilizing an electron blocking layer of TAPC Doped with MoO_3 [J]. Organic Electronics, 2019, 65: 150−155.

[72] RAHMANI A, REMACHE L, GUENDOUZ M, AIDA M S, HEBBOUL Z. Impact of the meso-PSi substrate on ZnO thin films deposited by spray pyrolysis technique for UV photodetectors [J]. Applied Physics A, 2021, 127: 396.

[73] CALISKAN D, BUTUN B, CAKIR M C, ÖZCAN Ş, OZBAY E. Low dark current and high speed ZnO metal–semiconductor–metal photodetector on SiO_2/Si substrate [J]. Applied Physics Letters, 2014, 105(16): 161108.

[74] ISMAIL R, AL-SAMARAI A M E, MOHAMMED W M. Preparation of n-ZnO/p-Si heterojunction photodetector via rapid thermal oxidation technique: Effect of oxidation time [J]. Materials Science, Chemistry Applied Physics A, 2018, 124(8): 527.

[75] KURNIAWAN F, RAHMI R. Synthesis of SnO_2 nanoparticles by high potential electrolysis [J]. Bulletin of Chemical Reaction Engineering & Catalysis, 2017, 12(2): 281−286.

[76] BOURAS D, FELLAH M, MECIF A, BARILLÉ R, OBROSOV A, RASHEED M. High photocatalytic capacity of porous ceramic-based powder doped with MgO [J]. Journal of the Korean Ceramic Society, 2023, 60: 155–168.

[77] BOURAS D, RASHEED M, BARILLE R, ALDARAJI M N. Efficiency of adding DD3+(Li/Mg) composite to plants and their fibers during the process of filtering solutions of toxic organic dyes [J]. Optical Materials, 2022, 131: 112725.

[78] BOURAS D, FELLAH M, BARILLE R, SAMAD M A, RASHEED M, ALRESHIDI M A. Properties of MZO/ ceramic and MZO/glass thin layers based on the substrate's quality [J]. Optical and Quantum Electronics, 2023, 56(1): 104.

[79] FELLAH M, HEZIL N, BOURAS D, OBROSOV A, MOHAMMED A S, MONTAGNE A, ABD-ELMONEM A, EL DIN S M, WEISS S. Structural, mechanical and tribological performance of a nanostructured biomaterial Co−Cr−Mo alloy synthesized via mechanical alloying [J]. Journal of Materials Research and Technology, 2023, 25: 2152−2165.

[80] WANG Da-yin, WANG Xiao-xiong, JIN Ming-liang, HE Peng, ZHANG Shu-ye. Molecular level manipulation of charge density for solid-liquid TENG system by proton irradiation [J]. Nano Energy, 2022, 103: 107819.

[81] CHEN J, ZHANG Z, LU H. Structure design and properties investigation of Bi_2O_2Se/graphene van der Waals hetero-junction from first-principles study [J]. Surfaces and Interfaces, 2022, 33: 102289.

[82] LU Ye-gang, STEGMAIER M, NUKALA P, GIAMBRA M A, FERRARI S, BUSACCA A, PERNICE W H P, AGARWAL R. Mixed-mode operation of hybrid phase-change nanophotonic circuits [J]. Nano Letters, 2017, 17(1): 150−155.

[83] YANG Sen-yuan, ZHANG Ying-fan, SHA Zhou, HUANG Zheng-yong, HAOHUAN Wang, WANG Fei-peng, LI Jian. Deterministic manipulation of heat flow via three-dimensional-printed thermal meta-materials for multiple protection of critical components [J]. ACS Applied Materials & Interfaces, 2022, 14(34): 39354−39363.

[84] WANG Jun, PAN Zeng-xi, WANG Yang-fan, WANG Long, SU Li-hong, CUIURI Dc, ZHAO Yu-hong, LI Hui-jun. Evolution of crystallographic orientation, precipitation, phase transformation and mechanical properties realized by enhancing deposition current for dual-wire arc additive manufactured Ni-rich NiTi alloy [J]. Additive Manufacturing, 2020, 34: 101240.

旋涂法制备电解和光电探测器用掺铁氧化锌薄膜

Dikra BOURAS[1], Mamoun FELLAH[2,3], Régis BARILLÉ[4],
Amjad IQBAL[5], Hamadi FOUZIA[3,6], Obrosov ALEKSEI[7], Gamal A. EL-HITI[8]

1. Faculty of Science and Technology, University of Souk-Ahras, Algeria;
2. Mechanical Engineering Department, ABBES Laghrour University, Khenchela PO 1252, CP 40004, Algeria;
3. Biomaterial, Synthesis and Tribology Research Team,
ABBES Laghrour-University, Khenchela, P.O 1252, 40004, Algeria;
4. MOLTECH-Anjou, Université d'Angers/UMR CNRS 6200, 2 Bd Lavoisier, 49045 Angers, France;
5. Department of Materials Technologies, Faculty of Materials Engineering,
Silesian University of Technology, Krasińskiego 8, 40-019, Katowice, Poland;
6. Matter Science Department, ABBES Laghrour University, Khenchela PO 1252, CP 40004, Algeria;
7. Brandenburg University of Technology Cottbus-Senftenberg, 03046, Cottbus, Germany;
8. Department of Optometry, College of Applied Medical Sciences, King Saud University, Riyadh 11433, Saudi Arabia

摘　要：探讨铁浓度对应用于电解和光电探测器的氧化锌显微组织和结构特性的影响。通过旋涂法在玻璃基底上沉积了未掺杂和掺杂不同含量铁(2%、4% 和 6%，质量分数)的氧化锌薄膜。采用 X 射线衍射(XRD)、原子力显微镜(AFM)、扫描电子显微镜(SEM)、能量色散 X 射线光谱(EDS)、紫外−可见吸收光谱以及 X 射线光电子能谱(XPS)等表征样品。XRD 结果表明，所有薄膜均为具有六方纤锌矿结构的多晶材料。掺杂后发现了两个新的衍射峰(400)和(440)，属于 Fe_2O_4 晶相。形貌分析显示，氧化锌薄膜的表面粗糙度为 8~45 nm。XPS 研究确认了氧化锌层中存在 Fe^{3+}。紫外光谱测量显示，在 200~900 nm 波长范围内，薄膜的平均透射率为 90%。随着铁浓度的增加，带隙(E_g)值逐渐减小。AFM 表面形貌分析表明，氧化锌薄膜具有相对均匀的表面。这些样品在包括光电探测器和污染溶液电解在内的多种电气应用的效率已得到验证。

关键词：Fe:ZnO；带隙；电解；光电探测；效率

(Edited by Bing YANG)